Upconversion-induced heat generation and thermal lensing in Nd:YLF and Nd:YAG

M. Pollnau,* P. J. Hardman, M. A. Kern, W. A. Clarkson, and D. C. Hanna
Optoelectronics Research Centre, University of Southampton, Southampton SO17 1BJ, United Kingdom
(Received 2 June 1998)

We investigate the influence of interionic upconversion between neighboring ions in the upper laser level of Nd:YLF and Nd:YAG on population dynamics, heat generation, and thermal lensing under lasing and nonlasing conditions. It is shown that cascaded multiphonon relaxations following each upconversion process generate significant extra heat dissipation in the crystal under nonlasing compared to lasing conditions. Owing to the unfavorable temperature dependence of thermal and thermo-optical parameters, this leads, first, to a significant temperature increase in the rod, second, to strong thermal lensing with pronounced spherical aberrations and, ultimately, to rod fracture in a high-power end-pumped system. In a three-dimensional finite-element calculation, excitation densities, upconversion rates, heat generation, temperature profiles, and thermal lensing are calculated. Differences in thermal lens power between nonlasing and lasing conditions up to a factor of 6 in Nd:YLF and up to a factor of 2 in Nd:YAG are experimentally observed and explained by the calculation. This results in a strong deterioration in performance when operating these systems in a *Q*-switched regime, as an amplifier, or on a low-gain transition. Methods to decrease the influence of interionic upconversion are discussed. It is shown that tuning of the pump wavelength can significantly alter the rod temperature.
[S0163-1829(98)04747-X]

I. INTRODUCTION

The Nd:YAG (Nd^{3+}:$Y_3Al_5O_{12}$) and Nd:YLF (Nd^{3+}:$LiYF_4$) transitions at 1.064 and 1.053 μm, respectively, have been widely used for laser applications, because they offer several advantages over other laser systems: The Nd^{3+} transition at 1 μm involves a four-level scheme with fast multiphonon transitions populating the upper and depleting the lower laser level. Its large stimulated-emission cross section allows a low laser threshold, while the small quantum defect allows high slope efficiency. YAG has a high fracture limit which is of advantage for use in high-power laser systems. YLF, on the other hand, is an attractive host material because of the wavelength match of the laser transition (1.053 μm) with Nd^{3+} glass amplifiers, the long storage time of the Nd^{3+} upper laser level, its natural birefringence, and its relatively weak thermal lensing on the polarization corresponding to 1.053 μm operation.[1] This weak lensing observed under lasing conditions is a consequence of YLF showing a decrease of refractive index with increasing temperature, creating a negative thermal lens, which partly compensates for the positive lens due to the bulging of the rod end faces. It gives Nd:YLF a significant advantage over Nd:YAG for power-scaling of diode-end-pumped systems into the multiwatt region while retaining an output beam of high spatial quality.[2–4]

However, under conditions of higher excitation density, such as nonlasing conditions, *Q*-switched operation, or operation as an amplifier, a strong deterioration in the performance of this seemingly simple system is observed. With increasing pump power and intensity, the Nd:YLF system exhibits a significantly reduced storage time under *Q*-switched operation and a decreasing laser efficiency.[5–7] This behavior has been explained by lifetime quenching owing to interionic upconversion processes involving two neighboring ions in the upper laser level.[8–10] As a consequence, Nd:YLF exhibits visible fluorescence from energy levels above the pump level. Furthermore, measurements of the induced thermal lens under lasing and nonlasing conditions demonstrate that significant additional heat is generated in the nonlasing situation, with the same pump power.[11] For Nd:YAG, similar effects of fluorescence quenching,[12,13] additional heat generation,[14,15] and increased thermal lensing[16] under nonlasing conditions have been observed.

The increased heat load has a number of undesirable consequences, such as spherical aberration in the thermally induced lens, with consequent degradation in laser-beam quality and higher resonator losses. Ultimately, with sufficient heat load, rod fracture will occur. With these effects being particularly pronounced under nonlasing conditions, it follows that *Q*-switched operation and operation as an amplifier will be especially susceptible. Therefore, an understanding of the mechanisms underlying the significant difference in heat dissipation under lasing and nonlasing conditions, and the resulting thermal lensing, is of great importance for the operation of these systems. Thermal lens calculations[17–27] have been performed mostly for Nd:YAG, but also for Nd:YLF and other materials. Those calculations have usually assumed a uniform heat input distribution or, if end-pumped, a radially Gaussian distribution and, in the longitudinal direction, an exponentially decaying heat input which was assumed to be a constant fraction of absorbed pump power. With this approach, it is not possible to explain the difference in thermal lensing observed under lasing and nonlasing conditions.[11,16]

In this paper, we carry out a spatially resolved investigation of the influence of the population dynamics on the heat load and thermal lensing behavior of the Nd:YLF and Nd:YAG systems under intense end-pumping for both lasing and nonlasing conditions. It is shown that interionic upcon-

version is responsible for significant additional heat load under nonlasing conditions and, in combination with the unfavorable temperature dependence of thermal and thermo-optical parameters, leads to a dramatic increase in thermal lens power and spherical aberration of the thermal lens under nonlasing conditions. Methods to decrease the influence of interionic upconversion are discussed.

In the following section, we shall investigate the way in which interionic upconversion influences the population dynamics of the system. In Sec. III, we shall discuss how the upconversion processes increase the heat dissipation. The temperature distributions that result from the given thermal input are derived and the influence of the pump spectral distribution is investigated. Section IV is devoted to the calculation of the thermal lensing behavior, a comparison with experimental results, and a discussion of the consequences of our results for certain operational regimes. The parameters of the experiments and simulations are presented in Appendix A and the equations implemented in the computer program are introduced in Appendix B.

II. POPULATION DYNAMICS

Detailed measurements of the thermal lensing behavior versus pump power under lasing and nonlasing conditions revealed that there is a significant increase in thermal lens powers under nonlasing compared to lasing conditions, with up to a factor of 6 observed in Nd:YLF (Ref. 11) and up to a factor of 2 in Nd:YAG.[16] To investigate this behavior, a computer source code was developed that allowed the three-dimensional calculation of heat generation, heat conduction, temperature distribution, and thermal lensing on the basis of the spatially resolved population dynamics of the system. The specific experimental situations referred to above[11,16] are the starting points of our numerical investigations.

In a computer simulation involving the relevant levels (ground state and eight excited states, see Fig. 1) and processes (pump power and configuration, ground-state absorption and depletion, all lifetimes and branching ratios, three interionic processes, stimulated emission, and the data of crystal and resonator), time- and space-dependent rate equations describing the Nd:YLF and Nd:YAG systems are solved numerically in order to obtain a quantitative understanding of our experimental results. For the tetragonal YLF system, a three-dimensional (tangential, sagittal, longitudinal) resolution is chosen, whereas the calculations for the cubic YAG system are performed with two-dimensional (radial, longitudinal) resolution. In these simulations the population dynamics are calculated and the heat generation, temperature distribution, and consequent thermal lensing behavior under lasing and nonlasing conditions are investigated.

In the experiments the radiation of a 20-W diode-laser bar was focused onto the crystal front surface, using a beam-shaping technique.[28] Pump details and details of laser mode size are given in Tables I and IV in Appendix A, respectively. The pump radiation was absorbed on the ground-state transition $^4I_{9/2} \rightarrow {}^4F_{5/2}$, see Fig. 1. The spectral distribution of the pump radiation is taken into account in the simulation. The spectral line shape is treated as Gaussian. The absorption cross sections in Nd:YLF are taken from the spectrum of Fig. 2. In our experiments,[11] the pump wavelength was significantly detuned from the Nd:YLF absorption peak at 797 nm, see Fig. 2, in order to prevent rod fracture. The corresponding spectrum of Nd:YAG is not shown. Since rod fracture is a minor problem in Nd:YAG under the chosen pump conditions, the pump wavelength was tuned directly onto the absorption peak at 809 nm in this host.[16]

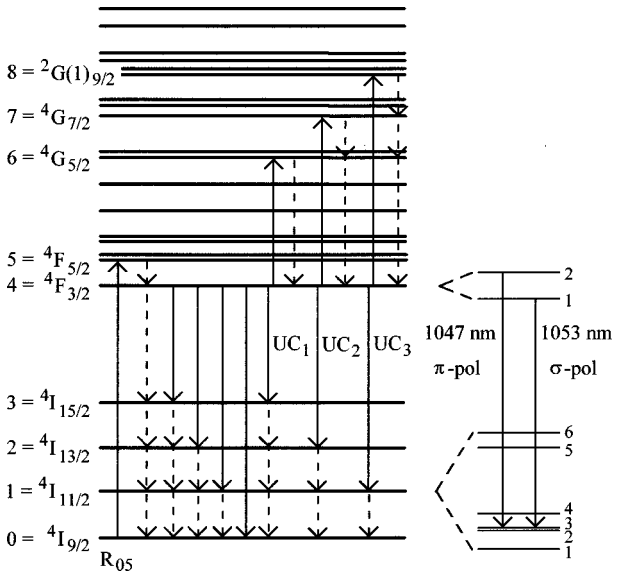

FIG. 1. Energy-level scheme of Nd:YLF indicating the dominant processes in the system: pump absorption with a rate R_{05}, multiphonon transition to the $^4F_{3/2}$ upper laser level, fluorescent transitions from the upper laser level, interionic upconversion processes UC_1-UC_3 from the upper laser level, cascaded multiphonon relaxations (dashed lines), and lasing Stark transitions in π and σ polarization. The important processes are the same in Nd:YAG, except for the details of the laser transition at 1064 nm.

The spatially resolved pump rate is calculated from Eqs. (B1)–(B6) of Appendix B, using the parameters of Tables I and II of Appendix A. At low pump power, i.e., if ground-state bleaching is absent, the absorbed fraction of the launched pump power is approximately 85% in the Nd:YLF

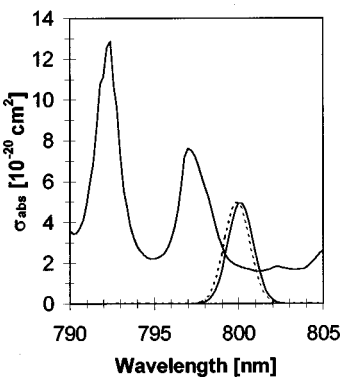

FIG. 2. Measured absorption spectrum of Nd:YLF for light polarized parallel to the crystal c axis (π polarization). Investigated spectral positions of the pump radiation emitted by the diode bar: normal position centered at 800.1 nm (solid line) and shift by 0.2 nm toward the absorption peak at 797 nm (dashed line). The spectral distribution of the diode emission is assumed to be of Gaussian shape.

crystal and 97% in the Nd:YAG crystal. At the highest incident pump powers of 12 W for Nd:YLF and 14.2 W for Nd:YAG, these values reduce to 79% and 95%, respectively, as a consequence of ground-state bleaching.

Concentration-dependent quenching of the lifetime of the Nd^{3+} $^4F_{3/2}$ level has been observed in several host materials. Three different cross-relaxation processes involving the $^4F_{3/2}$ and $^4I_{9/2}$ levels have been suggested[29–32] to be responsible for the observed behavior. If the population of the $^4I_{9/2}$ ground state is assumed to be independent of pump power, the corresponding depletion rate from the $^4F_{3/2}$ level will be linear with pump power and is thus incorporated in the measured lifetime of the $^4F_{3/2}$ level for the specific dopant concentration used in our experiment. If ground-state bleaching in taken into account, the decay rate introduced by the cross-relaxation processes is actually slightly less than linear with pump power.

Since the terminating levels $^4I_{15/2}$ and $^4I_{13/2}$ of these processes have extremely short lifetimes, it is of marginal importance for the population mechanisms of the system under nonlasing or cw lasing conditions whether the difference between the total decay rate and the sum of the radiative decay rates is due completely to multiphonon relaxation into the $^4I_{15/2}$ level, as in our assumption (cf. Appendix A and Table III), or partly to cross-relaxation processes. Both possibilities result in the excitation of one ion being transferred completely nonradiatively from the $^4F_{3/2}$ level to the ground state. The induced heat generation is also equivalent, i.e., these processes do not have to be considered separately in our rate equations; see later in Sec. III A. Evaluations of the specific contribution of concentration quenching to heat generation in Nd:YAG have been published in Refs. 32 and 33.

Interionic upconversion has been discussed in recent papers as a source of lifetime quenching in Nd:YLF under conditions of high excitation density.[8–10] Three upconversion processes UC_1-UC_3 (see Fig. 1) have been suggested[10] to contribute in a significant way to the population dynamics in Nd:YLF. These processes are considered in our simulation. The measured value for the parameter describing the influence of these combined upconversion processes, namely 1.7×10^{-16} cm^3/s,[8] was confirmed in an independent approach,[10] but with relatively high error margin. The estimated parameters of the individual interionic upconversion processes are given in Table III of Appendix A. The investigations of Ref. 10 indicate that the spectral overlap of the upconversion processes UC_1-UC_3 does not vary significantly with temperature in the range 250–500 K, hence a possible temperature dependence of the parameters of upconversion is not considered in the simulations.

Investigation of interionic upconversion in Nd:YAG (Refs. 8 and 34) resulted in published parameters which vary significantly in value. The value of the upconversion parameter of 5×10^{-17} cm^3/s (6900 s^{-1} for a dopant concentration of 1 at. %) determined in Ref. 34 was found to provide consistency of our experimental and calculated results for thermal lens powers.

It is apparent from Fig. 1 that, since levels 1 to 3 and 5 to 8 decay predominantly via fast multiphonon relaxation into their next lower-lying levels[10] and have a population density of $<10^{-6}$ of the dopant concentration, the effect of the three different processes UC_1-UC_3 on the population dynamics is similar (cf. the detailed discussion in Ref. 10). It is, therefore, of no great importance for our calculation which parameters of the individual upconversion processes are actually used in the rate equations as long as the sum of the parameters is equal to the parameters published for Nd:YLF (Refs. 8 and 10) and Nd:YAG (Ref. 34) (cf. also Sec. III for the influence of upconversion on heat dissipation).

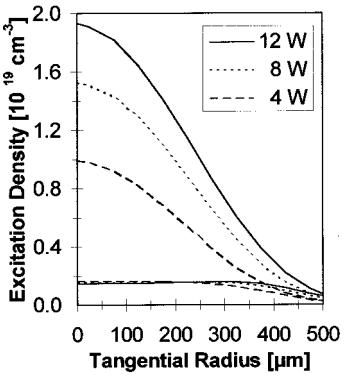

FIG. 3. Calculated excitation density for Nd:YLF within the front 5% of the crystal length versus tangential radius (pump-beam radius $w_{px0}=340$ μm, laser-beam radius $w_{lx}=300$ μm) for different pump powers of 12, 8, and 4 W under nonlasing (upper three curves) and lasing conditions (lower three curves).

The population densities of the levels which are denoted by a number and a spectroscopic term as well as the excitation and relaxation rates indicated in Fig. 1 are calculated from the rate-equation system (B7)–(B15) of Appendix B, using the spectroscopic parameters of Table III of Appendix A. The spatially resolved stimulated-emission rate on the laser transition $^4F_{3/2}\rightarrow{}^4I_{11/2}$, see Fig. 1, is calculated from Eqs. (B16)–(B19) of Appendix B, using the parameters of Table IV of Appendix A.

A. Excitation profiles

Since the $^4F_{3/2}$ upper laser level is the only level which has a long lifetime, significant excitation is accumulated only in this level. The excitation of this level depends on the transverse shape of the beam as well as the longitudinal distribution of the pump-power absorption, with the strongest excitation being found at the crystal front surface and in the center of the pump beam. In addition, the excitation depends on the conditions under which energy is extracted.

Under nonlasing conditions, the upper laser level is depleted by fluorescence and multiphonon relaxation as well as by interionic upconversion. The radial profiles of the excitation density in Nd:YLF at the crystal front surface for different pump powers are shown in Fig. 3 (upper three curves). The excitation does not rise linearly with pump power, because the upconversion rates and, thus, the depletion of the $^4F_{3/2}$ level increase nonlinearly with increasing excitation density. The radial excitation profile is almost Gaussian at lower pump powers, but becomes more super-Gaussian with increasing pump power, i.e., the relative increase in excitation is less pronounced in the center where the upconversion processes have a stronger influence.

Under lasing conditions, the excitation density of the upper laser level is clamped to laser threshold, see Fig. 3 (lower

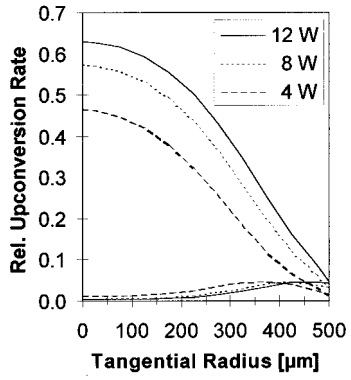

FIG. 4. Calculated relative upconversion rates for Nd:YLF with respect to pump rate within the front 5% of the crystal length versus tangential radius (pump-beam radius $w_{px0}=340\ \mu$m, laser-beam radius $w_{lx}=300\ \mu$m) for different pump powers of 12, 8, and 4 W under nonlasing conditions (upper three curves) and lasing conditions (lower three curves).

three curves). The excitation density in Nd:YLF at the highest pump power of 12 W is an order of magnitude smaller than under nonlasing conditions. It is also apparent that a laser-beam waist which is smaller than the pump-beam waist (as in the tangential direction shown in Fig. 3: pump-beam radius $w_{px0}=340\ \mu$m, laser-beam radius $w_{lx}=300\ \mu$m), does not extract the gain in the wings completely.

B. Upconversion rates

The transverse dependence of the upconversion rates per unit volume in Nd:YLF with respect to the pump rate is shown in Fig. 4 for different pump powers under nonlasing (upper three curves) and lasing conditions (lower three curves) at the crystal front surface. The difference of the excitation densities under nonlasing and lasing conditions of one order of magnitude at high pump power (Fig. 3) induces a difference in the upconversion rate which, as a consequence of its quadratic dependence on excitation density, is two orders of magnitude larger under nonlasing conditions compared to lasing conditions (Fig. 4).

Comparison of the upconversion rate with the pump rate provides an indication of the absolute influence of upconversion. The upconversion rate is defined here as the rate for a single ion, i.e., the depletion rate of the $^4F_{3/2}$ level population is twice this rate. Under nonlasing conditions, on the one hand, the upconversion rate reaches 63% in the center of the pump beam at the highest pump power. This means that the depletion rate of the $^4F_{3/2}$ level by upconversion is 126% of the pump rate, which is possible, because the half of the population which is upconverted to high-lying levels subsequently repopulates the $^4F_{3/2}$ level via multiphonon relaxation, thus introducing an additional excitation rate for this level of 63% of the real pump rate. Under lasing conditions, on the other hand, interionic upconversion has a marginal influence.

The additional depletion rate which is introduced to the $^4F_{3/2}$ upper laser level by interionic upconversion leads to a significant decrease in the lifetime of this level. Consequently, this reduces the storage capacity of the system under Q-switched operation or operation as an amplifier. This effect has been discussed in detail in Refs. 8 and 10.

III. HEAT GENERATION AND TEMPERATURE PROFILES

The main purpose of our investigation is to understand the nonlinearities which lead to the strong difference in thermal lens power measured under lasing and nonlasing conditions.[11,16] In this section, the processes that lead to heating of the Nd:YLF and Nd:YAG crystals are identified and the spatial temperature profiles are derived.

A. Heat generation

It is assumed in our calculation that pump absorption and fluorescent emission do not contribute directly to thermal loading of the rod by intramultiplet phonon relaxation, i.e., the actual Stark-level structures are neglected and the transitions are assumed to originate from and terminate in the lowest Stark levels of the corresponding multiplets. Thus, these processes contribute only indirectly to heat dissipation via subsequent multiphonon-relaxation processes into lower-lying multiplets, which are indicated by the dashed lines in Fig. 1.

Likewise, interionic upconversion processes only contribute indirectly to heat generation via subsequent multiphonon relaxation, because there is a direct spectral overlap for the corresponding emission and absorption lines,[10] hence these processes do not require assistance from an absorbed or emitted phonon. The total heat dissipation resulting from the cascaded multiphonon relaxations following each pair of processes (relaxation of one ion and excitation of its nearest-neighbor ion) is the same for the three individual processes and corresponds to one completely nonradiative relaxation from the upper laser level. The statement that only the sum of the parameters of the three interionic processes UC_1-UC_3 is of relevance for our investigation can, therefore, be extended to the thermal calculations.

The heat generated by cross relaxation and subsequent multiphonon decay from the upper laser level is also incorporated in our calculation, because concentration quenching of the intrinsic lifetime of the upper laser level is considered in the measured fluorescence lifetime and the additional decay rate is assumed to be nonradiative. This leads to a quantitatively correct contribution from concentration quenching, as long as the amount of ground-state bleaching is small.

Thus, the thermal load of the crystal is due solely to the cascaded multiphonon relaxations indicated by the dashed lines in Fig. 1. Data of the eight individual processes are summarized in Table V of Appendix A for the case of Nd:YLF. The spatially resolved heat load of the crystal is calculated from Eq. (B20) of Appendix B.

We first investigate the thermal power generated under lasing conditions. If the excitation density is clamped to threshold, interionic upconversion has a marginal influence and the upper laser level is depleted almost completely on the laser transition, i.e., the multiphonon transitions $^4F_{3/2} \rightarrow {}^4I_{15/2} \rightarrow {}^4I_{13/2} \rightarrow {}^4I_{11/2}$ can be neglected. The thermal load can then be calculated from the sum of the contributions of the multiphonon relaxations from pump level to upper laser level, $^4F_{5/2} \rightarrow {}^4F_{3/2}$, and from lower laser level to ground state, $^4I_{11/2} \rightarrow {}^4I_{9/2}$ (as indicated in Table V of Appendix A) or, equally, from the Stokes efficiency of the system. For Nd:YLF, 24% of absorbed pump power is converted to heat.

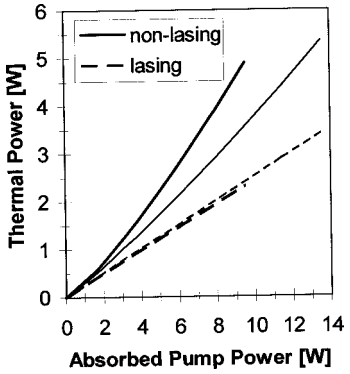

FIG. 5. Calculated thermal power dissipated in the whole crystal versus absorbed pump power under nonlasing and lasing conditions for Nd:YLF (thick lines) and Nd:YAG (thin lines). The data under nonlasing conditions are not directly comparable, because the pump-waist areas are $340\times220\ \mu\mathrm{m}^2$ in Nd:YLF and $225\times225\ \mu\mathrm{m}^2$ in Nd:YAG, leading to a different influence of upconversion under nonlasing conditions.

This result is independent of pump power, if the laser threshold is low. This finding is in agreement with the result obtained from the solution of the full rate-equation system, see Fig. 5, which is 2.3 W of thermal load for 9.5 W of absorbed power in Nd:YLF.

Under nonlasing conditions, the situation is much more complicated. When calculating the heat generated by the linear relaxation rates, the branching ratios from the $^4F_{3/2}$ level (see Table III of Appendix A) have to be taken into account. In Nd:YLF, a fraction of $\gamma_{43}\beta_{43}=0.034$ is assumed to decay via multiphonon relaxation from the upper laser level to the next lower-lying level and further via multiphonon processes to the ground state, i.e., all four processes $^4F_{3/2}\rightarrow{}^4I_{15/2}\rightarrow{}^4I_{13/2}\rightarrow{}^4I_{11/2}\rightarrow{}^4I_{9/2}$ generate heat in this case. This rate includes the part that decays via cross relaxation. A fraction of $(1-\gamma_{43})\beta_{43}=0.006$ decays via fluorescence on the transition $^4F_{3/2}\rightarrow{}^4I_{15/2}$ and generates heat only via the latter three processes, a fraction of β_{42} decays via fluorescence on the transition $^4F_{3/2}\rightarrow{}^4I_{13/2}$ and generates heat via the latter two processes, etc. This results in the relative strengths of the above four multiphonon processes as indicated in Table V of Appendix A. When neglecting interionic processes, the result is that 25% of absorbed pump power would be converted to heat, which is similar to the fraction under lasing conditions.

The same investigation in Nd:YAG leads to a similar fraction of 25% under lasing conditions, but the corresponding fraction of heat generation owing to linear processes under nonlasing conditions would increase to more than 29%. This is because of the larger phonon energies in YAG as well as additional nonradiative quenching channels,[12,13,15,29,30,32,33] resulting in an increased nonradiative rate from the $^4F_{3/2}$ upper laser level and a correspondingly smaller fluorescence lifetime in Nd:YAG.

However, the upconversion processes lead to a relative increase in the rates of the multiphonon processes compared to predominantly fluorescent decay and, in addition, induce the processes $^2G(1)_{9/2}\rightarrow{}^4G_{7/2}\rightarrow{}^4G_{5/2}\rightarrow{}^4F_{5/2}\rightarrow{}^4F_{3/2}$. Therefore, the heat dissipation calculated from the full rate-equation system under nonlasing conditions deviates significantly from the values of 25% in Nd:YLF or 29% in Nd:YAG, see Fig. 5, and increases nonlinearly with pump power. In Nd:YLF 4.9 W of thermal load for 9.5 W of absorbed pump power is generated under nonlasing conditions, i.e., 52% or more than twice the amount of heat compared to lasing conditions. The result for Nd:YAG, 40% or 5.4 W of thermal load for 13.5 W of absorbed pump power under nonlasing conditions, is less pronounced (Fig. 5), because the fluorescence decay time is shorter, i.e., the linear processes are stronger, and the upconversion parameter is smaller in Nd:YAG compared to Nd:YLF.

B. Temperature profiles

The large amount of pump-induced heating requires cooling of the laser crystal. This is usually realized by radial heat transfer from the crystal surface to a cooling element, e.g., a water-cooled copper block, e.g., using a layer of indium foil to enhance thermal contact between crystal and a cooling element. This requires a radial temperature gradient from the rod center. Consequently, the crystal forms a thermally induced lens. In this section, the temperature profiles produced by the Gaussian pump shape, the nonlinear heat dissipation, the temperature-dependent thermal conductivity, and the radial cooling are calculated.

The importance of the temperature dependence of the thermal conductivity for the resulting temperature profiles has recently been pointed out by a number of authors.[23,24,26,35] Thermal resistance at ambient temperature and above arises owing to phonon-phonon scattering. Since the number of phonons increases linearly with temperature, the thermal conductivity varies with temperature as $1/T$. For a more detailed description, cf. Ref. 36. Generally, the thermal conductivity has a small dependence on the doped ion.[37] Radial convective cooling by a copper heat sink and surface convective cooling by air are assumed in the calculation. Convective air cooling at the rod end faces is found to have only a small influence in the calculation.

With Eqs. (B21)–(B27) of Appendix B and the parameters of Table VI of Appendix A, the temperature distribution in the whole rod is calculated under lasing and nonlasing conditions for different pump powers. The sagittal and longitudinal temperature profiles in Nd:YLF at the highest absorbed power of 9.5 W are shown in Figs. 6(a) and 6(b). The largest temperature increase is found at the crystal front surface in the center of the pump beam where the strongest absorption occurs. Whereas the temperature increase from the coolant temperature of 288 K does not exceed 45 K under lasing conditions, see Fig. 6(b), the increase under nonlasing conditions is more than 115 K at the point of highest pump absorption, see Fig. 6(a). Consequently, the temperature gradient is much more pronounced under nonlasing conditions.

The corresponding temperature increase in Nd:YAG for 9.5 W of absorbed power is only 37 and 62 K under lasing and nonlasing conditions, respectively. At the highest absorbed power of 13.5 W, the increase is 54 and 95 K, respectively. The larger temperature increase in Nd:YLF is a result of the smaller thermal conductivity in this host and the larger contribution of upconversion under nonlasing conditions. The temperature dependence of the thermal conductivity further increases the temperature in the Nd:YLF rod.

We include the spectral distribution of the diode pump power in our calculation, cf. Eqs. (B1)–(B6) of Appendix B

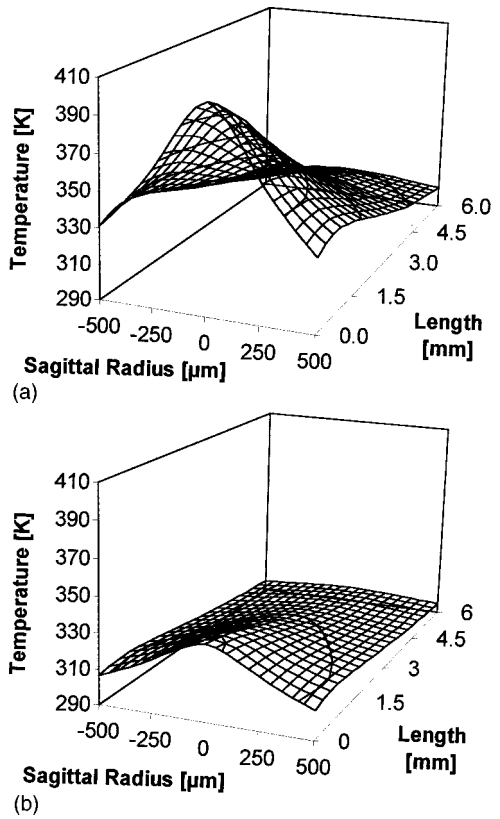

FIG. 6. Calculated temperature profiles for Nd:YLF versus sagittal radius (pump-beam radius $w_{py0}=220\ \mu$m, laser-beam radius $w_{ly}=300\ \mu$m) under (a) nonlasing and (b) lasing conditions. The radial boundary given by the rod radius is $r_b=\pm 2$ mm. Owing to convective radial cooling by a water-cooled copper block, the temperature at the boundary is elevated from the radial coolant temperature of $T_{br}=288$ K by a few K.

and Table II of Appendix A. Since the absorption cross section changes with pump wavelength, the absorption length may vary significantly over the spectral pump distribution. In Nd:YLF, the pump wavelength was significantly detuned from the absorption peak at 797 nm, see Fig. 2, in order to prevent rod fracture.

Now we consider a situation where the spectral emission of the diode pump power is temperature tuned by only 0.2 nm toward the absorption peak at 797 nm (dashed line in Fig. 2). Since the major part of the pump power is in a spectral region where the absorption cross section changes only slightly with pump wavelength, the total absorption of the incident pump power of 12 W increases only from 79% to 80% under nonlasing conditions. This is a tiny effect and would hardly be noticed in a direct way in the experiment, but the consequences for temperature, stress, and strain in the rod are much more pronounced. A small part of the pump power at the short-wavelength side of the pump spectrum is shifted to a wavelength region of strong absorption, cf. Table II of Appendix A, and is now absorbed within the front part of the crystal. The calculation shows that, with all the nonlinearities involved, the temperature in Nd:YLF at the front surface in the center of the pump beam increases from 404 to 414 K, thus strongly increasing stress and strain in this area and, ultimately, posing an increased risk of rod fracture.

IV. THERMAL LENSING

As shown in our calculation in Sec. III, the temperature varies strongly with radial position owing to the Gaussian pump profile, the change of the linear population mechanisms, and heat generation by upconversion under nonlasing conditions, as well as the radial cooling of the active medium. This temperature profile induces strong thermal lensing in the crystal.

A. Thermal dispersion, thermal expansion, stress, and strain

Three different effects are generally important in this context. First, the refractive index of the host material changes with temperature, which leads to differences in longitudinal optical path lengths through the rod across the transverse temperature profile, thus introducing a lens whose power has the same sign as the change of refractive index with temperature. Second, the crystal expands with temperature and the resulting bulging of the rod end faces defines a lens which has the same sign as the expansion of the crystal along the resonator axis. Third, the nonuniform expansion leads to stress in the crystal, which also changes the refractive index, leading to stress-induced birefringence. It is the purpose of this section to calculate values for the thermal lens for the different population dynamics and heat generation under lasing and nonlasing conditions and to compare these results with experimentally obtained data.

Since the temperature increase in the rod is significant under high-power end pumping, a knowledge of the temperature dependence not only of the thermal conductivity but also of the thermo-optical parameters is important. The change in refractive index with temperature, dn/dT, is itself a function of temperature, which, for YAG, is nearly linear over the temperature range of interest around 300 K. Since temperature-dependent data, d^2n/dT^2, were not available for YLF, we have assumed the same qualitative temperature dependence for both crystal axes in YLF (see Appendix A for details of these assumptions).

At room temperature and above, the expansion coefficient also increases almost linearly with temperature. In a simple model,[36] the temperature dependence of the expansion coefficient depends mainly on the temperature dependence of the specific heat, which can be calculated from the Debye function. The measured temperature dependence of the expansion coefficient in YAG is in reasonable agreement with this model. Again, temperature-dependent data were not available for YLF and the dependence is estimated from the data available for YAG, which is justified by the model. For details, cf. Appendix A and Eqs. (B28) and (B29) of Appendix B.

The third effect, the stress-induced birefringence, is not considered in our calculation. It is believed to be of minor importance in YLF,[23] because this material shows a strong natural birefringence.

Stress and strain also have an influence on the expansion of the crystal. Equation (B29) of Appendix B as well as the data of the expansion coefficient presented in Appendix A rely on the free expansion of the crystal in one direction. If a transversely localized temperature increase occurs (e.g., end-pumping with a Gaussian profile), the heated element cannot freely expand in the longitudinal direction, because it is con-

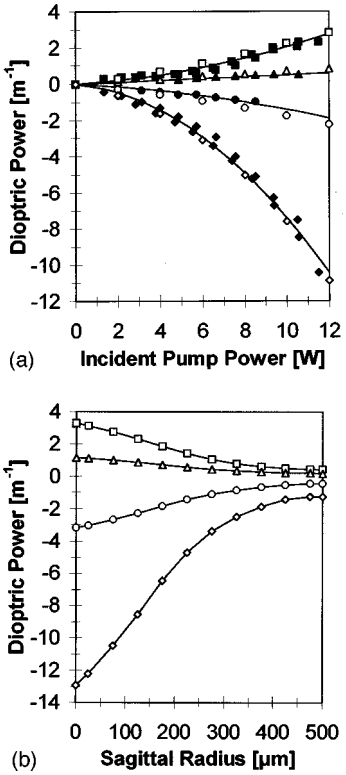

FIG. 7. Nd:YLF: (a) Dioptric power of the thermal lens versus incident pump power along the crystal *a* axis and (b) variation of dioptric power (spherical aberration) of thermal lensing versus radius along the crystal *a* axis at the highest incident pump power of 12 W: experimental data (solid symbols), taken from Ref. 11, and calculated data (open symbols), in σ polarization under nonlasing (squares) and lasing (triangles) conditions as well as in π polarization under nonlasing (diamonds) and lasing (circles) conditions.

strained by its colder surrounding. We make the simplifying assumption that Eq. (B29) of Appendix B is modified by stress and strain to Eq. (B30), where the parameter C_α takes account of this constraint. The above assumption results in the contribution of the bulging having the same radial dependence as the temperature distribution. In practice, the shape of the bulge will probably differ from this profile due to the modifications introduced by stress and strain, but this first-order approximation is more realistic than assuming free expansion.

C_α is treated as the only free parameter in all the calculations presented in this paper. It is adjusted in order to match a single measured value, the value of the thermal lens power at highest pump power under nonlasing conditions in π polarization along the YLF *a* axis. It is kept at a constant value for all calculations. This does not introduce a general degree of freedom to the calculations, as will become apparent later from Fig. 7(a). Since the contributions to thermal lensing due to the change in refractive index and bulging have opposite signs and since the former exceeds the latter for π polarization, but the reverse is true for σ polarization, resulting in thermal lenses of opposite sign for π and σ polarization, the variation of C_α does not allow for an adjustment of the calculated magnitude of the thermal lens power in both π and σ polarizations. With increasing C_α the thermal lens becomes stronger in σ polarization, but it simultaneously becomes weaker in π polarization and vice versa. In addition, a fixed value of C_α has no direct influence on the pump-power dependence of the thermal lens power, nor can it help in adjusting the difference of the thermal lensing under lasing and nonlasing conditions. The same value of C_α is used for the calculations in Nd:YAG.

B. Thermal lens powers and aberrations

In YLF there are four principal values of thermal lens, depending on the choice of polarization, π or σ, and on the choice of lens axis, tangential or sagittal. In our experiment the crystal is oriented with its *c* axis parallel to the tangential plane. π and σ denote the polarizations parallel and perpendicular to the crystal *c* axis, respectively.

Measurements of thermal lensing in Nd:YLF have been reported by several authors.[3,4,11,23] In Ref. 11, the thermal lens powers were measured versus incident pump power under lasing and nonlasing conditions. The measurements provided values of the thermal lens power averaged over the transverse dimension of the laser or probe beam. Under lasing conditions, the output characteristics of the laser beam itself, which had a beam radius of 300 μm inside the rod, was investigated, whereas under nonlasing conditions the transmitted light of a He-Ne probe beam, which had a beam radius of 150 μm inside the rod, was used for the detection of the thermal lens. The measurements in Nd:YAG (Ref. 16) were carried out interferometrically. The experimental parameters were identical to those presented in Appendix A. These parameters were used to calculate the thermal lens powers according to Eqs. (B28)–(B37) of Appendix B.

The experimental (solid symbols) and calculated results (open symbols) for the *a* axis in Nd:YLF are shown in Fig. 7(a). The thermal lens power under lasing conditions increases almost linearly with pump power. The contribution to the thermal lens power from the change in refractive index with temperature is negative. For π polarization, its absolute value is larger than that from the bulging of the rod end faces, resulting in negative thermal lens powers. For σ polarization, the contribution from the change in refractive index with temperature is smaller in absolute value and the bulging effect predominates, resulting in a positive sign of the thermal lens.

Under nonlasing conditions, the additional heat generated by the upconversion processes as well as the unfavorable temperature dependencies of thermal conductivity and thermo-optical parameters lead to a thermal lens whose power increases nonlinearly with pump power. At the highest pump power of 12 W, the thermal lens power under nonlasing conditions compared to lasing conditions is almost six times stronger in π polarization and almost five times stronger in σ polarization. The difference in this factor for the two polarizations is a consequence of the different temperature dependence of the change in refractive index and thermal expansion coefficient. The agreement between experimental and calculated results is excellent, indicating that the major contributions to heat generation and thermal lensing for the *a* axis have been identified.

The measured thermal lens power parallel to the *c* axis (tangential plane) is much weaker than that perpendicular to the *c* axis (sagittal plane),[11] which is partly due to the larger pump-waist radius in the tangential resonator plane (340 μm compared to 220 μm in the sagittal plane) and partly due to

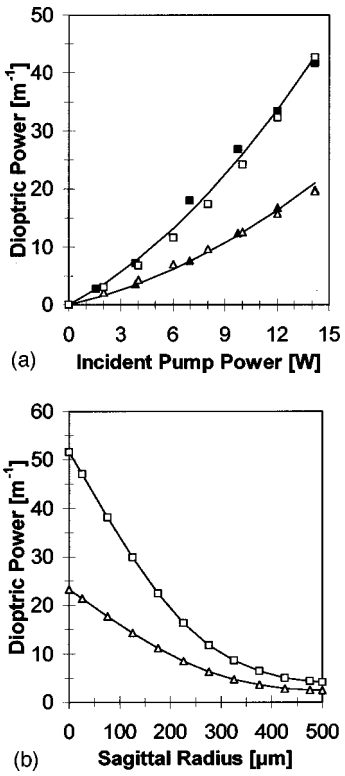

FIG. 8. Nd:YAG: (a) Dioptric power of the thermal lens versus incident pump power and (b) variation of dioptric power (spherical aberration) of thermal lensing versus radius at the highest incident pump power of 14.2 W: experimental data (solid symbols), taken from Ref. 16, and calculated date (open symbols), under nonlasing (squares) and lasing (triangles) conditions.

reasons yet unknown to us. The measured thermal lens power parallel to the *c* axis is less accurately reproduced in the simulation, with the calculated values being larger than the measured values.

A possible reason for the difference in thermal lens powers along the two crystal axes could be a much larger anisotropy in the thermal conductivity for *a* and *c* axis than reported in Ref. 38 (cf. Table VI of Appendix A). When treating the thermal conductivity in *a*- and *c*-axis direction as free parameters, we find from our calculations that the thermal conductivity along the *c* axis must be more than a factor of 2 larger than along the *a* axis in order to reproduce the difference in thermal lens powers as obtained from the measurements. A single influence of either the change of refractive index with temperature or the bulging of the rod end faces can be excluded as a reason, because it would lead to thermal lens values which are more positive or negative for both π and σ polarization. The experimental results[11] show instead a decrease of the absolute values for both π and σ polarization.

The experimental results (solid symbols) of Ref. 16 and calculated results (open symbols) for Nd:YAG are shown in Fig. 8(a). Since the YAG system is cubic, the behavior for tangential and sagittal planes as well as for the corresponding polarizations are identical, and the behavior is described by only one curve for lasing condition and one for nonlasing.

Generally, the thermal lens powers are greater for Nd:YAG compared to Nd:YLF, cf. Figs. 8(a) and 7(a), because, first, the parameter which makes the main contribution, namely the change in refractive index with temperature, is much larger in YAG than in YLF, and, second, the contributions of change in refractive index and expansion have the same sign in YAG and hence add, in contrast to the case for YLF. In addition, the absorbed pump intensity at the crystal front surface was twice as large in the Nd:YAG experiment. On the other hand, the thermal conductivity is higher in YAG, which leads to smaller peak temperatures, thus reducing the runaway effect of the thermal conductivity decreasing with increasing temperature. As in Nd:YLF, the thermal lens power under nonlasing conditions is larger than under lasing conditions, but the effect is less pronounced in Nd:YAG, because the fluorescence decay time is shorter and the upconversion parameter is smaller in Nd:YAG compared to Nd:YLF, which leads to a smaller influence of upconversion in Nd:YAG.

The spherical aberrations of the thermal lens along the Nd:YLF *a* axis for the highest pump power of 12 W are shown in Fig. 7(b). Under nonlasing conditions, the aberrations are much more pronounced than under lasing conditions. Similar results are obtained for Nd:YAG at the highest pump power of 14.2 W, see Fig. 8(b). Since the thermal lens powers are generally larger in Nd:YAG compared to Nd:YLF, also the aberrations over the pump-beam radius are significantly larger in Nd:YAG under lasing as well as nonlasing conditions.

These strong aberrations can lead to a distortion of the Gaussian shape of the fundamental laser mode, with a consequent degradation in laser-beam quality and higher resonator losses. If part of the aberrated thermal lens, e.g., the strongest lens in the rod center, leads to a partly unstable resonator, this will also result in higher resonator losses.

In certain situations, all the nonlinearities involved may introduce a runaway effect. Higher resonator losses result in higher threshold inversion, which quadratically increases upconversion rates. This leads to extra heat generation and a higher temperature, which decreases the thermal conductivity, thus further increasing the temperature. This results in stronger thermal lensing and lens aberration, which is worsened by the unfavorable temperature dependence of the thermo-optical parameters. In return, this introduces even higher resonator losses, and further instability will be highly pronounced. At a critical power level, a small increase in pump power may thus lead to a dramatic change in the behavior of the laser system. A proper resonator design which avoids even small resonator losses is, therefore, of extreme importance in order to operate such a laser at high output power in a transversely fundamental mode.

C. Consequences for certain operational regimes

It becomes apparent from the investigations of this paper that the problems of heat generation, thermal lensing, and lens aberration increase significantly if the system is operated in a regime of higher excitation density, i.e., in a *Q*-switched regime, as an amplifier, or on a low-gain transition, because upconversion plays a larger role in these regimes, with all the consequences discussed above.

Generally, the best way to limit the influence of interionic upconversion is to use a smaller dopant concentration. This decreases energy migration within the initial level of the upconversion process and hence the possibility of two excita-

tions to meet at the nearest-neighbor distance. Thus, the upconversion parameter decreases. In addition, the excitation density under the same pump conditions is smaller. However, this measure implies that a longer rod is used in order to maintain the fraction of pump power which is absorbed in the rod. If also the absorbed pump intensity is a critical parameter, this requires a pump source with correspondingly high brightness, i.e., small M^2 values.

A second possibility which underlies the same restriction concerning the pump source is to tune the pump to a wavelength with smaller absorption cross section, which also decreases the excitation density. This measure is less powerful than the first, because it does not simultaneously decrease the upconversion parameter. Third, the influence of upconversion can also be decreased by focusing to a larger pump-waist size.

Under *Q*-switched operation, where the pump intensity is less critical, all these methods can be applied. When operating the system as an amplifier, a high pump intensity is essential for efficient amplification. The pump beam cannot be defocused and a high-brightness pump source is essential in order to apply one of the first two methods. Since no stable resonator has to be established for the signal beam, the quenching of the storage time of the $^4F_{3/2}$ level by upconversion[8,10] may be a more important problem in the amplifier situation than thermal lensing.

Besides these consequences for specific operational regimes, there are several practical consequences involved with upconversion-induced heat generation. First, if a cw Nd:YAG or Nd:YLF laser operates at high pump power, misalignment of the resonator leads to significant extra heat generation and an increase in rod temperature within a time scale of about a second, resulting in an increased risk of rod fracture.

Second, because of the stronger thermal lensing under nonlasing conditions, a certain resonator may become unstable under these conditions at the highest pump power, whereas it remains stable under lasing conditions. Thus, in order to operate such a laser at the highest pump power, the laser has to be started at medium pump power, where the resonator is stable under nonlasing as well as lasing conditions, and then the pump can be switched to higher power. We have observed this effect in a 946-nm Nd:YAG laser system, which generates less heat than a 1.064-μm system and, consequently, exhibits an even larger difference in fractional heat dissipation and thermal lensing under lasing and nonlasing conditions.

Independently of specific-heat-generating mechanisms such as upconversion, it is advantageous to choose a small rod radius and a low cooling temperature in order to keep the temperature in the rod center at a lower level. This decreases the runaway effects which result from the unfavorable temperature dependence of thermal and thermo-optical parameters.

V. CONCLUSIONS

The thermal lensing in high-power diode-end-pumped Nd:YLF and Nd:YAG rods was investigated in experiments and calculations. The experiments reported in Refs. 11 and 16 showed a significant difference in thermal lensing under lasing and nonlasing conditions. In order to understand these findings, a computer source code was developed that allowed the three-dimensional calculation of heat generation, heat conduction, temperature distribution, and thermal lensing on the basis of the spatially resolved population mechanisms of the system.

Interionic upconversion processes from the $^4F_{3/2}$ level and subsequent cascaded multiphonon relaxation were found to be responsible for a significant increase in heat generation in Nd:YLF from 24% of the absorbed pump power under lasing conditions up to 52% under nonlasing conditions, for a maximum absorbed pump power of 9.5 W. In Nd:YAG, corresponding values are 25% and 40%, for 13.5 W of absorbed pump power. The additional heat load increases nonlinearly with pump power. Taking into account the unfavorable temperature dependence of the thermal conductivity, this leads to an increase in temperature in Nd:YLF at the point of highest pump absorption from 332 K under lasing conditions to 404 K under nonlasing conditions, when setting the coolant temperature to 288 K. Corresponding temperature values in Nd:YAG are 342 and 383 K, respectively. Owing to the spectral distribution of the diode pump power, tuning of the diode emission wavelength may lead to a significant increase in temperature, stress, and strain. Thus small changes in the overall absorbed pump power can lead to a significantly worsened risk of rod fracture.

Thermal lens powers were calculated in Nd:YLF for the crystal *a*- and *c*-axis direction and for π and σ polarization under lasing and nonlasing conditions. For the *a* axis, calculated results are in excellent agreement with experimental data. The thermal lens power depends almost linearly on pump power under lasing conditions, whereas, under nonlasing conditions a strongly nonlinear behavior is measured and calculated, caused by upconversion as well as the temperature dependence of thermal and thermo-optical parameters. Thermal lens powers up to a factor of 6 larger were observed under nonlasing compared to lasing conditions. The significantly weaker thermal lensing for the crystal *c* axis has as yet not been understood. It might be caused by a larger anisotropy in the thermal conductivity than has been reported in the literature.

Generally, there is not sufficient information on thermal and thermo-optical parameters in the YLF host. The temperature dependence of the thermal and thermo-optical parameters as well as the components of the strain and elasto-optical tensors will have to be measured accurately and the thermally induced stress and strain will have to be included in the simulation in order to provide a more detailed understanding of thermal lensing in the YLF host.

In Nd:YAG, the observed increase in thermal lens power from lasing to nonlasing conditions was only a factor of 2 because of the stronger linear decay rates and the smaller upconversion parameter compared to Nd:YLF. However, thermal lens powers are generally higher than in Nd:YLF, because in YAG the change in refractive index with temperature is larger and the resulting contribution to thermal lensing has the same sign as the contribution from the bulging of the rod end faces. At our highest available input powers, under nonlasing conditions, focal lengths of the thermal lens as small as 2 cm have been found for Nd:YAG, compared to 9 cm for Nd:YLF.

TABLE I. Crystal and pump data.

Crystal	YLF	Ref.	YAG	Ref.
Density ρ (10^3 kg m^{-3})	3.99	39	4.55	40 and 41
Specific heat C_p (J K^{-1} kg^{-1})	790	2	607	40 and 42
Debye temp. T_D (K)			750	37 and 43
Length l_c (mm)	6	Expt.	10	Expt.
Radius r_b (mm)	2	Expt.	1.5	Expt.
Nd^{3+} conc. N_d (10^{20} cm^{-3})	1.59	Expt.	1.52	Expt.
(at. % on Y^{3+} site)	(1.15)		(1.1)	
Orientation of c axis	$\parallel x$ axis	Expt.		
Polarization of pump light	$\parallel x$ axis	Expt.		
Diode pump power P_{in} [W]	20	Expt.	20	Expt.
Coupling efficiency η_{in}	0.60	Expt.	0.71	Expt.
abs. fraction of $\eta_{\text{in}}P_{\text{in}}$				
at low pump power	0.85	Expt.	0.97	Expt.
at highest pump power	0.79		0.95	
Pump focus w_{p0} (μm)				
Tangential plane (x axis)	340	Expt.	225	Expt.
Sagittal plane (y axis)	220	Expt.	225	Expt.
Beam-quality factor M^2				
Tangential plane (x axis)	79	Expt.	75	averaged
Sagittal plane (y axis)	63	Expt.	75	averaged

The additional heat generation introduces a strong spherical aberration of the thermal lens, resulting in decreased beam quality of the laser output as well as increased resonator losses, thus further enhancing heat generation and thermal lensing.

The effects discussed in this paper lead to a strong deterioration in performance when operating the system under conditions of higher excitation density, e.g., in a Q-switched regime, as an amplifier, or on a low-gain transition. Possible measures to reduce the detrimental influence of interionic upconversion include increasing the pump-waist size, detuning the pump wavelength from a region of strong absorption, and using a longer rod with smaller dopant concentration.

ACKNOWLEDGMENTS

The authors thank Wolfram Schöne from the Laser Zentrum Hannover, Germany, for helpful discussions concerning the thermal lens calculations. Parts of the source code were developed during earlier work at the Institute of Applied Physics, University of Bern, Switzerland. M.P. was supported by the European Union within the ''Human Capital and Mobility Programme.'' P.J.H. acknowledges the support of Lumonics, Ltd.

APPENDIX A: PARAMETERS AND VALUES

This appendix explains all parameters which are relevant for the computer calculations and provides all values used in the simulations.

In Table I, the data of the Nd:YLF and Nd:YAG crystals as well as the data of the pump beams are summarized. Absorbed fractions of the launched pump power at low input power are experimental data which are reproduced in the calculations. Absorbed fractions at high pump power are determined from the calculations and take into account ground-state bleaching. M^2 values of the pump beam in the Nd:YAG experiment are averaged from the values measured along the tangential and sagittal planes.

TABLE II. Spectral distributions of the diode pump power in the experiments investigating Nd:YLF (upper eight rows) and Nd:YAG (lower five rows).

No.	$\lambda(i)$ (nm)	$P_{\text{in},\lambda(i)}/P_{\text{in}}$ (%)	$\sigma_{p,\lambda(i)}$ (10^{-20} cm^2)	$\sigma_{s,\lambda(i)}$ (10^{-20} cm^2)
1	798.8	6.1	3.30	3.85
2	799.2	8.6	2.40	2.80
3	799.5	14.4	2.10	2.40
4	799.9	20.9	1.85	2.00
5	800.3	20.9	1.75	1.85
6	800.7	14.4	1.70	1.75
7	801.0	8.6	1.70	1.70
8	801.4	6.1	1.75	1.70
1	808.0	16	2.6	
2	808.5	21	3.3	
3	809.0	26	4.6	
4	809.5	21	2.0	
5	810.0	16	1.3	

Table II provides the spectral distribution of the diode pump power in the experiments investigating Nd:YLF (upper eight rows) and Nd:YAG (lower five rows). The temperature-stabilized pump wavelengths are centered at $\lambda_p = 800.1$ and 809.0 nm, respectively. The spectral linewidths are approximately $\Delta\lambda = 3$ nm. For the simulations, the spectral pump shape is assumed to be Gaussian, and eight (or five) individual spectral parts centered at wavelength $\lambda(i)$ are calculated. Also given are the fractional power $P_{\text{in},\lambda(i)}/P_{\text{in}}$ and the absorption cross section $\sigma_{p,\lambda(i)}$ of each part, as derived from the spectrum of Fig. 2 (Nd:YLF) or from the corresponding spectrum of Nd:YAG. If, in the Nd:YLF experiment, the diode is temperature-tuned by $\Delta\lambda_s = 0.2$ nm toward the absorption peak at 797 nm, the individual absorption cross sections are shifted toward the values $\sigma_{s,\lambda(i)}$.

In Table III, the spectroscopic parameters of Nd:YLF and Nd:YAG are presented. The intrinsic lifetimes of upper and lower laser level are given in the table. The lifetimes τ_i of the other excited levels have been discussed in Ref. 10 for Nd:YLF and are assumed here as $\tau_i \sim 20$ ns for Nd:YLF and Nd:YAG. The branching ratios β_{4i} from the $^4F_{3/2}$ upper laser level are calculated from Judd-Ofelt data for the radiative transition rates in Nd:YLF (Ref. 47) and Nd:YAG (Ref. 48) and from the fluorescence lifetime τ_4 with the procedure used in Ref. 49. This procedure assumes that the difference between the total intrinsic decay rate τ_4^{-1} and the sum of the radiative decay rates is due to multiphonon relaxation into the next lower-lying level $^4I_{15/2}$. The nonradiatively emitted fraction of the rate from the $^4F_{3/2}$ upper laser level into the next lower-lying level is given by γ_{43}, i.e., the branching ratio β_{43} splits into a radiative part $(1-\gamma_{43})\ \beta_{43}$ and a non-

TABLE III. Spectroscopic parameters of Nd:YLF and Nd:YAG.

Crystal	Nd:YLF	Ref.	Nd:YAG	Ref.
Lifetimes (μs)				
Upper laser level: τ_4 (Nd^{3+} conc. 1 at. %)	520	44	230	39
Lower laser level: τ_1	0.02	45 and 46	0.0002	46
Branching ratios				
${}^4F_{3/2}\rightarrow{}^4I_{15/2}$: β_{43}	0.040	this Ref.	0.114	this Ref.
Nonradiative fraction: γ_{43}	0.858	this Ref.	0.970	this Ref.
${}^4F_{3/2}\rightarrow{}^4I_{13/2}$: β_{42}	0.115	this Ref.	0.113	this Ref.
${}^4F_{3/2}\rightarrow{}^4I_{11/2}$: β_{41}	0.523	this Ref.	0.446	this Ref.
${}^4F_{3/2}\rightarrow{}^4I_{9/2}$: β_{40}	0.322	this Ref.	0.327	this Ref.
Upconversion (10^{-16} cm^3 s^{-1})				
UC_1: W_1	0.01	10		
UC_2: W_2	0.26	10		
UC_3: W_3	1.43	10		
$W=W_1+W_2+W_3$	1.7	8 and 10	0.5	34

radiative part $\gamma_{43}\,\beta_{43}$. All other excited levels are assumed to decay nonradiatively into their next lower-lying level (cf. Ref. 10 and references therein) and further to the ground state or to the ${}^4F_{3/2}$ upper laser level, which is indicated by the dashed lines in Fig. 1.

Table IV lists the parameters of the laser transitions in Nd:YLF and Nd:YAG. The measured effective stimulated-emission cross section is the atomic cross section weighted by the Boltzmann factor of the upper Stark laser level. P denotes the product of spectral and spatial fraction of fluorescence coupled into the TEM_{00} laser mode. The resonator losses are adjusted in the simulation in order to reproduce the output powers measured in the experiments.

Table V provides data on the eight individual multiphonon processes that lead to heat generation in the Nd:YLF crystal, their rate-equation terms $\vartheta_i(\mathbf{r})$, the energy gaps ΔE_i that have to be bridged by these processes, and the fractions of absorbed pump energy transformed into heat by the individual processes under nonlasing and lasing conditions, both under the theoretical assumption that upconversion processes are absent. It is assumed that each relaxation takes place from lowest to lowest Stark level of the involved multiplets. The total fractions of deexcitation via multiphonon processes under nonlasing and lasing conditions are calculated as the sum of all contributions with respect to the energy of a pump photon of 12 500 cm^{-1}. Corresponding values for Nd:YAG are given in Sec. III. The Stark-level energies are taken from the summary in Ref. 10. The energy of the lowest Stark level of the ${}^4F_{5/2}$ multiplet (not included in Ref. 10) is 12 533 cm^{-1}.[51]

In Table VI values of the parameters used for the calculation of the temperature profiles and thermal lenses in YLF and YAG are summarized. The values for Θ are derived from the values of K_C, using Eq. (B25) of Appendix B.

TABLE IV. Parameters of the laser transitions in Nd:YLF and Nd:YAG.

Crystal	YLF			YAG	
Polarization	π-pol	σ-pol	Ref.		Ref.
Upper Stark laser level	2	1		2	
Lower Stark laser level	3	3		3	
Wavelength λ_l (nm)	1047	1053		1064	
Boltzmann factor b_4 (300 K)	0.427	0.573		0.384	
Boltzmann factor b_1 (300 K)	0.113	0.113		0.186	
Eff. emission cross section (10^{-19} cm^2)	1.9	1.4	44	4.6	50
Atomic cross section σ_l (10^{-19} cm^2)	4.45	2.44		12.0	
Degeneracy g_4	2	2		2	
Degeneracy g_1	2	2		2	
Fraction P	10^{-11}	10^{-11}		10^{-11}	
Optical resonator length l_{opt} (mm)	136	136	Expt.	143	Expt.
Double-pass losses L (%)	1.0	1.0		1.8	
Mirror reflectance in/out Rf (%)	100/90	100/90	Expt.	100/97	Expt.
TEM_{00} laser-beam radius w_l (μm)	300	300	Expt.	200	Expt.

TABLE V. Multiphonon processes in Nd:YLF. The contribution of each process under nonlasing conditions is calculated from the branching ratios of relaxations from the upper laser level, under neglect of the influence of interionic upconversion. Under lasing conditions, it is assumed that decay from the upper laser level occurs only via stimulated emission on the laser transition.

Process	Rate-equation term	Multiphonon energy	Nonlasing	Lasing
$^2G(1)_{9/2}\rightarrow{}^4G_{7/2}$	$\vartheta_8(\mathbf{r})=\tau_8^{-1}N_8(\mathbf{r})$	$\Delta E_8=1961\ \mathrm{cm}^{-1}$	0.0%	0.0%
$^4G_{7/2}\rightarrow{}^4G_{5/2}$	$\vartheta_7(\mathbf{r})=\tau_7^{-1}N_7(\mathbf{r})$	$\Delta E_7=1901\ \mathrm{cm}^{-1}$	0.0%	0.0%
$^4G_{5/2}\rightarrow{}^4F_{5/2}$	$\vartheta_6(\mathbf{r})=\tau_6^{-1}N_6(\mathbf{r})$	$\Delta E_6=4621\ \mathrm{cm}^{-1}$	0.0%	0.0%
$^4F_{5/2}\rightarrow{}^4F_{3/2}$	$\vartheta_5(\mathbf{r})=\tau_5^{-1}N_5(\mathbf{r})$	$\Delta E_5=995\ \mathrm{cm}^{-1}$	100.0%	100.0%
$^4F_{3/2}\rightarrow{}^4I_{15/2}$	$\vartheta_4(\mathbf{r})=\gamma_{43}\beta_{43}\tau_4^{-1}N_4(\mathbf{r})$	$\Delta E_4=5690\ \mathrm{cm}^{-1}$	3.4%	0.0%
$^4I_{15/2}\rightarrow{}^4I_{13/2}$	$\vartheta_3(\mathbf{r})=\tau_3^{-1}N_3(\mathbf{r})$	$\Delta E_3=1901\ \mathrm{cm}^{-1}$	4.0%	0.0%
$^4I_{13/2}\rightarrow{}^4I_{11/2}$	$\vartheta_2(\mathbf{r})=\tau_2^{-1}N_2(\mathbf{r})$	$\Delta E_2=1950\ \mathrm{cm}^{-1}$	15.5%	0.0%
$^4I_{11/2}\rightarrow{}^4I_{9/2}$	$\vartheta_1(\mathbf{r})=\tau_1^{-1}N_1(\mathbf{r})$	$\Delta E_1=1997\ \mathrm{cm}^{-1}$	67.8%	100.0%
		Total fraction	25.0%	23.9%

For many of the thermal and thermo-optical parameters of Nd:YAG, several values have been found in the literature. The value of the thermal conductivity of 12 $\mathrm{W\,K^{-1}\,m^{-1}}$ is averaged from the values of 9.76,[40] 10,[38] 10.5,[35] 12.9,[40] 13,[2,23,24,42] 13–14,[43] and 14 $\mathrm{W\,K^{-1}\,m^{-1}}$.[39] Published values of heat-transfer coefficients are 1,[20,26,39] 1.14–11.4,[52] and 7.5×10^4 $\mathrm{W\,K^{-1}\,m^{-2}}$ (Ref. 23) from crystal to water and 6.5,[52] 10,[20] and 27.5 $\mathrm{W\,K^{-1}\,m^{-2}}$ (Refs. 21 and 23) from crystal to air. We use values of 1×10^4 $\mathrm{W\,K^{-1}\,m^{-2}}$ for heat transfer from crystal via copper to water and 6.5 $\mathrm{W\,K^{-1}\,m^{-2}}$ for heat transfer from crystal to air in our calculations.

The refractive index n_r is taken from Refs. 23, 24, 39, and 42. Published data of the change in refractive index with temperature, $n_r'=dn_r/dT$, at room temperature are 7,[2] 7.2,[40] 7.3,[23,39] 8.3,[24] 8.9,[38] and 9.86×10^{-6} $\mathrm{K^{-1}}$.[42,21] We use the value of Ref. 24, because this reference provides temperature-dependent data, from which we calculate the value of $n_r''=dn_r'/dT=2.6\times10^{-8}$ $\mathrm{K^{-2}}$.

Room-temperature data of the expansion coefficient α_T' are 5.8,[35] 6.7,[38] 6.95,[40] 7–8,[2] 7.3–7.7,[43] 7.5,[24,53] 7.7–8.2,[39] 8.2,[23] and 8.9×10^{-6} $\mathrm{K^{-1}}$.[54] We use the recently published value of Ref. 35, because this reference provides temperature-dependent data, from which we calculate the value of the almost linear increase of α_r' with temperature of $\alpha_T''=d\alpha_T'/dT=1.25\times10^{-8}$ $\mathrm{K^{-2}}$, (cf. the value of 1.625×10^{-8} $\mathrm{K^{-2}}$ derived from the data of Refs. 24 and 39). Published values of Poisson's ratio are 0.25 (Ref. 35) and 0.30.[23]

In the model of Ref. 36, the expansion coefficient is proportional to the Grüneisen parameter and the specific heat which both depend on temperature. Since the Grüneisen parameter increases only slightly for temperatures approaching the Debye temperature T_D (750 K in YAG[37,43]), the temperature dependence of the expansion coefficient is mostly determined by the temperature dependence of the specific heat, which is given by the Debye function. At room temperature or $0.4T_D$, the Debye function increases with a slope of 1.4×10^{-3} $\mathrm{K^{-1}}$, in reasonable agreement with the value of $\alpha_T''/\alpha_T'=2.2\times10^{-3}$ $\mathrm{K^{-1}}$ derived from the data of Ref. 35.

TABLE VI. Values of the parameters used for the calculation of the temperature profiles and thermal lenses in YLF and YAG. The temperature dependencies of the YLF values denoted with an asterisk are estimated from the corresponding dependence in YAG.

Crystal	YLF			YAG	
Axis	*c* axis	*a* axis	Ref.		Ref.
Thermal conductivity					
K_C (300 K) ($\mathrm{W\,K^{-1}\,m^{-1}}$)	5.8	7.2	38	12	averaged
T-independent Θ ($\mathrm{W\,m^{-1}}$)	1740	2160		3600	
Temp. of radial heat sink T_{br} (K)	288		Expt.	288	Expt.
Transfer coeff. Cu K_{Tr} ($\mathrm{W\,m^{-2}}$)	1×10^4			1×10^4	20, 26, and 27
Temp. of long. heat sink T_{bz} (K)	293		Expt.	293	Expt.
Transfer coeff. air K_{Tz} ($\mathrm{W\,m^{-2}}$)	6.5			6.5	52
Refractive index n_r	1.470	1.448	23 and 39	1.82	23, 24, 39, and 42
$dn_r/dT=n_r'$ (300 K) (10^{-6} $\mathrm{K^{-1}}$)	−4.3	−2.0	2, 23, and 38	8.3	24
$dn_r'/dT=n_r''$ (10^{-8} $\mathrm{K^{-2}}$)	−1.3*	−0.63*		2.6	24
Expansion coeff.					
α_T' (300 K) (10^{-6} $\mathrm{K^{-1}}$)	8	13	2, 23, 38, and 39	5.8	35
$d\alpha_T'/dT=\alpha_T''$ (10^{-8} $\mathrm{K^{-2}}$)	1.73*	2.82*		1.25	35
Scaling factor C_α	0.35			0.35	
Poisson's ratio ν	0.33		23 and 39	0.25	35

The remaining part can be attributed to the temperature dependence of the Grüneisen parameter.

Values of the thermal conductivity in YLF,[38] measured in *a*- and *c*-axis direction at room temperature, of $K_{Ca}=7.2\ \mathrm{W\,K^{-1}\,m^{-1}}$ and $K_{Cc}=5.8\ \mathrm{W\,K^{-1}\,m^{-1}}$, respectively, are used in the calculation (cf. the value of $K_C=6\ \mathrm{W\,K^{-1}\,m^{-1}}$,[2,23,39,55] with no indication of a dependence on crystal axis given in those references). Values of $n_r'=dn_r/dT$ at $T_0=300$ K, for the two crystal axes in YLF, are $n_{rc}'(T_0)=-4.3\times10^{-6}\ \mathrm{K^{-1}}$ and $n_{ra}'(T_0)=-2.0\times10^{-6}\ \mathrm{K^{-1}}$ (Refs. 2, 23, and 38) [cf. the values of $n_{rc}'(T_0)=-3.0\times10^{-6}\ \mathrm{K^{-1}}$ and $n_{ra}'(T_0)=-0.8\times10^{-6}\ \mathrm{K^{-1}}$ (Ref. 55)].

Several temperature-dependent data of YLF could not be found in literature. These values are estimated from the corresponding temperature dependence in YAG and are denoted with an asterisk in Table VI. Experimental data may differ from these values. We use the slope n_r'' measured for YAG and redimension it for YLF by multiplying with the factors $n_{rc}'(\mathrm{YLF})/n_r'(\mathrm{YAG})=-0.52$ and $n_{ra}'(\mathrm{YLF})/n_r'(\mathrm{YAG})=-0.24$, respectively. It is thus assumed that the qualitative function $n_r'(T)$ in YLF is similar to that in YAG, but the absolute values of n_r' are adjusted for the case of YLF. Resulting values for YLF are $n_{rc}''=-1.3\times10^{-8}\ \mathrm{K^{-2}}$ and $n_{ra}''=-0.63\times10^{-8}\ \mathrm{K^{-2}}$. The same procedure applies for the expansion coefficient. Values in YLF at room temperature are $\alpha_{Tc}'(T_0)=8\times10^{-6}\ \mathrm{K^{-1}}$ and $\alpha_{Ta}'(T_0)=13\times10^{-6}\ \mathrm{K^{-1}}$.[2,23,38,39] Recalculation of the temperature dependence for YLF yields estimated values of $\alpha_{Tc}''=1.73\times10^{-8}\ \mathrm{K^{-2}}$ and $\alpha_{Ta}''=2.82\times10^{-8}\ \mathrm{K^{-2}}$.

APPENDIX B: EQUATIONS

In this appendix, all equations of the computer model are explained for the calculation with three-dimensional (tangential, sagittal, longitudinal) resolution which was used in the case of the tetragonal system Nd:YLF. The equations for two-dimensional (radial, longitudinal) resolution used in the case of the cubic system Nd:YAG are somewhat easier and have partly been published in Ref. 10. They shall not be presented here. Parameters are explained in Appendix A.

x, *y*, and *z* are the variables of tangential, sagittal, and longitudinal coordinate within the crystal, respectively. They represent the discrete longitudinal elements $z=1$ to n covering the crystal length l_c as well as the discrete transverse elements $x,y=1$ to m covering twice the maximum pumped radii $w_{px,y}(z=n)$ in tangential and sagittal planes, respectively, at the position of the last longitudinal element at the crystal back surface. A finite-element resolution of $n=8$ and $m=10$ is chosen for the calculation, providing 800 finite elements for the calculation of the population dynamics. Further spatial elements covering the remaining outer part of the crystal are implemented for the calculation of thermal flux and temperature. The radial rod boundary is approximated by the squared finite elements. The calculated volume covers one quadrant of the transverse area. Several of the equations following in the remainder of this appendix must be multiplied by a factor of 4 in order to take account of the full transverse area.

The geometry of the spatial resolution is denoted by $\mathbf{r}=(x,y,z)$, the space vector, $r=(x,y)$, its transverse part, $x_1(r)$, $y_1(r)$ and $x_2(r)$, $y_2(r)$ the inner and outer transverse borders of the spatial element, its lengths $\Delta x(r)=x_2(r)-x_1(r)$ and $\Delta y(r)=y_2(r)-y_1(r)$, $\Delta l(z)$, the length of the longitudinal element *z*, and $\mathrm{vol}(\mathbf{r})=\Delta x(r)\Delta y(r)\Delta l(z)$, the volume of the spatial element at $\mathbf{r}$. $\Delta\overline{x}(rr')$, $\Delta\overline{y}(rr')$, and $\Delta\overline{l}(zz')$ are the distances between the centers of adjacent spatial elements located at $\mathbf{r}$ and $\mathbf{r}'$.

1. Rate equations

The absorption coefficients $\alpha_{\lambda(i)}(\mathbf{r})$ of the individual spectral parts *i* of the pump beam at wavelength $\lambda(i)$ within the spatial element at $\mathbf{r}$ are

$$\alpha_{\lambda(i)}(\mathbf{r})=\sigma_{p,\lambda(i)}N_0(\mathbf{r}), \tag{B1}$$

where $N_0(\mathbf{r})$ is the population density of the ground state. The pump-beam radii in tangential and sagittal resonator plane (with the waist radii w_{px0} and w_{py0} at the crystal front surface $z=0$) are given by

$$w_{px/y}^2(z)=w_{px0/y0}^2+\left[\frac{zM_{x,y}^2\lambda_p}{\pi n_{rc/a}w_{px0/y0}}\right]^2. \tag{B2}$$

The fraction $\rho_p(\mathbf{r})$ of the power of the Gaussian pump beam contained in the spatial element at $\mathbf{r}$ compared with the total pump power in the longitudinal element *z* is

$$\rho_p(\mathbf{r})=\frac{2}{\pi w_{px}(z)w_{py}(z)}\int_{x_1(r)}^{x_2(r)}\exp\left(\frac{-2x'^2}{w_{px}^2(z)}\right)dx' \times\int_{y_1(r)}^{y_2(r)}\exp\left(\frac{-2y'^2}{w_{py}^2(z)}\right)dy'. \tag{B3}$$

The Gaussian integrals in Eq. (B3) do not possess an analytical solution for arbitrary boundaries and must be solved numerically. The power $P_{p,\lambda(i)}(z)$ which is launched into the longitudinal element *z* is calculated as

$$P_{p,\lambda(i)}(z)=\eta_{\mathrm{in}}P_{\mathrm{in},\lambda(i)}\prod_{z'=1}^{z-1}\left\{\sum_{x',y'=1}^{m}[\rho_p(\mathbf{r}')\exp(-\Delta l(z')\alpha_{\lambda(i)}(\mathbf{r}'))]\right\}. \tag{B4}$$

It is an implication of Eqs. (B3) and (B4) that after absorption of the pump power in each longitudinal element a Gaussian pump shape is maintained, i.e., a possible degradation of the Gaussian pump shape due to ground-state bleaching and, therefore, radially non-uniform absorption is neglected. With Eqs. (B1)–(B4), the equations for the pump rates $R_{\lambda(i)}(\mathbf{r})$ of the spectral parts i of the pump power per unit volume from the ground state into the $^4F_{5/2}$ level read:

$$R_{\lambda(i)}(\mathbf{r})=\{1-\exp[-\Delta l(z)\alpha_{\lambda(i)}(\mathbf{r})]\}\,\frac{\lambda_p}{hc}\,\frac{P_{p,\lambda(i)}(z)\rho_p(\mathbf{r})}{\mathrm{vol}(\mathbf{r})}. \tag{B5}$$

h and c denote Planck's constant and the vacuum speed of light, respectively. The resulting pump rate $R_{05}(\mathbf{r})$ for absorption on the ground-state transition $^4I_{9/2}$ (level 0) $\rightarrow{}^4F_{5/2}$ (level 5),

$$R_{05}(\mathbf{r})=\sum_{i=1}^{k} R_{\lambda(i)}(\mathbf{r}), \tag{B6}$$

is the sum of the $k=8$ individual pump rates $R_{\lambda(i)}(\mathbf{r})$. The rate equations for the population densities $N_i(\mathbf{r})$ read

$$dN_8(\mathbf{r})/dt=W_3N_4^2(\mathbf{r})-\tau_8^{-1}N_8(\mathbf{r}), \tag{B7}$$

$$dN_7(\mathbf{r})/dt=W_2N_4^2(\mathbf{r})+\tau_8^{-1}N_8(\mathbf{r})-\tau_7^{-1}N_7(\mathbf{r}), \tag{B8}$$

$$dN_6(\mathbf{r})/dt=W_1N_4^2(\mathbf{r})+\tau_7^{-1}N_7(\mathbf{r})-\tau_6^{-1}N_6(\mathbf{r}), \tag{B9}$$

$$dN_5(\mathbf{r})/dt=R_{05}(\mathbf{r})+\tau_6^{-1}N_6(\mathbf{r})-\tau_5^{-1}N_5(\mathbf{r}), \tag{B10}$$

$$dN_4(\mathbf{r})/dt=\tau_5^{-1}N_5(\mathbf{r})-\tau_4^{-1}N_4(\mathbf{r})-2(W_1+W_2+W_3)N_4^2(\mathbf{r})-S_{\pi/\sigma}(\mathbf{r}), \tag{B11}$$

$$dN_3(\mathbf{r})/dt=\beta_{43}\tau_4^{-1}N_4(\mathbf{r})-\tau_3^{-1}N_3(\mathbf{r})+W_1N_4^2(\mathbf{r}), \tag{B12}$$

$$dN_2(\mathbf{r})/dt=\beta_{42}\tau_4^{-1}N_4(\mathbf{r})+\tau_3^{-1}N_3(\mathbf{r})-\tau_2^{-1}N_2(\mathbf{r})+W_2N_4^2(\mathbf{r}), \tag{B13}$$

$$dN_1(\mathbf{r})/dt=\beta_{41}\tau_4^{-1}N_4(\mathbf{r})+\tau_2^{-1}N_2(\mathbf{r})-\tau_1^{-1}N_1(\mathbf{r})+W_3N_4^2(\mathbf{r})+S_{\pi/\sigma}(\mathbf{r}), \tag{B14}$$

$$N_d=\sum_{i=0}^{8} N_i(\mathbf{r}). \tag{B15}$$

For the calculation of the stimulated-emission rate, the following considerations are made. Thermal redistribution within the multiplets takes place instantaneously. Since the temperature profile of the active material is calculated in the simulation, the Boltzmann distributions of upper and lower Stark laser levels are considered with spatial resolution. The fraction $\rho_l(\mathbf{r})$ of the photon number of the Gaussian laser beam contained in the spatial element at $\mathbf{r}$ compared with the total photon number in the longitudinal element z is

$$\rho_l(\mathbf{r})=\frac{2}{\pi w_{lx}(z)w_{ly}(z)}\int_{x_1(r)}^{x_2(r)}\exp\left(\frac{-2x'^2}{w_{lx}^2(z)}\right)dx'\int_{y_1(r)}^{y_2(r)}\exp\left(\frac{-2y'^2}{w_{ly}^2(z)}\right)dy'. \tag{B16}$$

In the low-gain approximation, the rate equation for the photon number $\phi_{\pi/\sigma}$ in the resonator for π and σ polarization, respectively, is given by

$$d\phi_{\pi/\sigma}/dt=\frac{l_c}{l_{\mathrm{opt}}}\sum_{z=1}^{n}\left\{\sum_{x,y=1}^{m}[P\beta_{41}\tau_4^{-1}N_4(\mathbf{r})+S_{\pi/\sigma}(\mathbf{r})]\mathrm{vol}(\mathbf{r})\right\}-\{-\ln[Rf_1Rf_2(1-L)]\}\,\frac{c}{2l_{\mathrm{opt}}}\,\phi_{\pi/\sigma}, \tag{B17}$$

where $S_{\pi/\sigma}(\mathbf{r})$ is the stimulated-emission rate on the laser transition,

$$S_{\pi/\sigma}(\mathbf{r})=[b_{4,\pi/\sigma}(T(\mathbf{r}))N_4(\mathbf{r})-(g_{4,\pi/\sigma}/g_1)b_1(T(\mathbf{r}))N_1(\mathbf{r})]\times\frac{\sigma_{l,\pi/\sigma}}{\Delta x(r)\Delta y(r)}\,\frac{c}{2l_{\mathrm{opt}}}\,\rho_l(\mathbf{r})\phi_{\pi/\sigma}. \tag{B18}$$

The output power P_{out} on the laser transition can be calculated from the equation

$$P_{\mathrm{out},\pi/\sigma}=\frac{c}{2l_{\mathrm{opt}}}\,(1-Rf_2)\,\frac{hc}{\lambda_{l,\pi/\sigma}}\,\phi_{\pi/\sigma}. \tag{B19}$$

After the initial determination of Eqs. (B2), (B3), and (B16), Eqs. (B1), (B4)–(B15), (B17), and (B18) are solved in a Runge-Kutta calculation of fourth order.

2. Heat generation and temperature profiles

The dissipated thermal power $Q_{\mathrm{th}}(\mathbf{r})$ in each spatial element is calculated from the multiphonon rates according to Table V of Appendix A, using the equation

$$Q_{\mathrm{th}}(\mathbf{r})=\sum_{i=1}^{8}\Delta E_i\vartheta_i(\mathbf{r})\mathrm{vol}(\mathbf{r}), \tag{B20}$$

where the ΔE_i of Table V of Appendix A have been converted to SI units by $\Delta E_i(J)=100hc\Delta E_i\ (\mathrm{cm}^{-1})$. The three-dimensional thermal conduction is considered for the calculation of the temperature distribution in the laser rod, taking into account the anisotropy in the thermal conductivity for the YLF host. With the power of the thermal flux for the tangential, sagittal, and longitudinal directions given by

$$P_{\mathrm{th},x}(\mathbf{r}) = -K_{Cc}(T(\mathbf{r}))\Delta l(z)\Delta y(r)[\Delta T_x(\mathbf{r}'\mathbf{r})/\Delta\overline{x}(r'r) - \Delta T_x(\mathbf{r}\mathbf{r}'')/\Delta\overline{x}(rr'')], \tag{B21}$$

$$P_{\mathrm{th},y}(\mathbf{r}) = -K_{Ca}(T(\mathbf{r}))\Delta l(z)\Delta x(r)[\Delta T_y(\mathbf{r}'\mathbf{r})/\Delta\overline{y}(r'r) - \Delta T_y(\mathbf{r}\mathbf{r}'')/\Delta\overline{y}(rr'')], \tag{B22}$$

$$P_{\mathrm{th},z}(\mathbf{r}) = -K_{Ca}(T(\mathbf{r}))\Delta x(r)\Delta y(r)[\Delta T_z(\mathbf{r}'\mathbf{r})/\Delta\overline{l}(z'z) - \Delta T_z(\mathbf{r}\mathbf{r}'')/\Delta\overline{l}(zz'')], \tag{B23}$$

and with Eq. (B20), the equation for the thermal conduction[56] reads

$$\partial T(\mathbf{r})/\partial t = \frac{1}{C_p\rho\ \mathrm{vol}(\mathbf{r})}\,[Q_{\mathrm{th}}(\mathbf{r}) + P_{\mathrm{th},x}(\mathbf{r}) + P_{\mathrm{th},y}(\mathbf{r}) + P_{\mathrm{th},z}(\mathbf{r})]. \tag{B24}$$

Here $\Delta T(\mathbf{r}'\mathbf{r})$ is the difference between the temperatures $T(\mathbf{r}')$ and $T(\mathbf{r})$ at the centers of two adjacent spatial elements at $\mathbf{r}'$ and $\mathbf{r}$, respectively, in the direction $(\mathbf{r}'\rightarrow\mathbf{r})$ of the power $P_{\mathrm{th}}(\mathbf{r})$ of the thermal flux. The convention for the sign of $\Delta T(\mathbf{r}'\mathbf{r})$ is such that power $P_{\mathrm{th}}(\mathbf{r})$ flowing into the spatial element at $\mathbf{r}$ has a positive sign. At room temperature and above, the temperature dependence of the thermal conductivity of a crystalline material is sufficiently well described by the general law[36]

$$K_{Cc/a}(T(\mathbf{r})) = \Theta_{c/a}/T^{\delta}(\mathbf{r}), \tag{B25}$$

where the parameter δ depends on the host material and is usually in the range $(1,\ldots,2)$. Experimental results for YAG (cf. Refs. 22 and 57 and references therein) suggest $\delta\approx 1$ around 300 K. This value is also used as an approximation in our calculation for YLF. Radial convective cooling by a water-cooled copper heat sink and convective air cooling at the rod end faces is assumed. The radial and longitudinal boundary conditions are[20,26,56]

$$\partial T(\mathbf{r})/\partial \mathbf{n}_{r/z} = \frac{K_{Tr/z}}{K_{Cc/a}(T(\mathbf{r}))}\,[T(\mathbf{r}) - T_{br/z}], \tag{B26}$$

with the heat flux being directed parallel to the normal $\mathbf{n}_{r/z}$ of the surface. For a small finite element at location $\mathbf{r}$ at, e.g., the tangential surface, the heat flux through the surface is assumed as

$$\partial T(\mathbf{r})/\partial t = -\frac{K_{Tr}}{C_p\rho\ \mathrm{vol}(\mathbf{r})}\,\Delta l(z)\Delta y(r)[T_{br} - T(\mathbf{r})]. \tag{B27}$$

Equation (B27) does not take into account a possible difference in surface heat-transfer coefficient K_{Tr} along the crystal a and c axis of YLF, because data of the transfer coefficient are not available for this material.

3. Thermal lensing

The change in refractive index with temperature, $n_r' = dn_r/dT$, is itself a function of temperature. According to experimental results for YAG,[24] we make the linear approximation

$$n'_{rc/a}(T(\mathbf{r})) = n'_{rc/a}(T_0) + n''_{rc/a}[T(\mathbf{r}) - T_0]. \tag{B28}$$

According to experimental data for YAG,[35] the temperature dependence of the expansion coefficient α_T', which is the parameter of one-dimensional free expansion, is also assumed to be linear:

$$\alpha'_{Tc/a}(T(\mathbf{r})) = \alpha'_{Tc/a}(T_0) + \alpha''_{Tc/a}[T(\mathbf{r}) - T_0]. \tag{B29}$$

We make the simplifying assumption that Eq. (B29) is modified by stress and strain according to

$$\alpha'_{Tc/a}(T(\mathbf{r})) = C_{\alpha}\{\alpha'_{Tc/a}(T_0) + \alpha''_{Tc/a}[T(\mathbf{r}) - T_0]\}. \tag{B30}$$

Here C_α is a parameter varying in the range $(0,\ldots,1)$. It takes into account that, if a transversely localized temperature increase occurs, the heated element cannot freely expand in the longitudinal direction, because it is constrained by its colder surrounding.

The change in refractive index leads to the following contribution of the spatial element at $\mathbf{r}$ to the optical path difference for radiation polarized in π or σ polarization:[19,20,23,26,27]

$$O_{n',\sigma/\pi}(\mathbf{r}) = n'_{rc/a}(T(\mathbf{r}))T(\mathbf{r})\Delta l(z). \tag{B31}$$

Since in the YLF experiment the longitudinal axis is one of the two a axes of the crystal, the contribution of the spatial element at $\mathbf{r}$ to the optical path difference induced by end-face bulging is given by[19,20,23,26,27]

$$O_{\alpha'}(\mathbf{r}) = (n_{ra} - 1)(1+\nu)\alpha'_{Ta}(T(\mathbf{r}))T(\mathbf{r})\Delta l(z), \tag{B32}$$

with α'_{Ta} from Eq. (B30). In the paraxial approximation, the transverse shape of the optical path difference for a beam traveling in the longitudinal direction is calculated from Eqs. (B31) and (B32), and

$$O_{\sigma/\pi}(r) = \sum_{z=1}^{n} O_{n',\sigma/\pi}(\mathbf{r}) + O_{\alpha'}(\mathbf{r}). \tag{B33}$$

We fit a value of a spherical lens to each spacing between two transversely adjacent finite elements in order to derive the thermal lens power with transverse resolution. A spherical thermal lens at radial position r is described by the equations[58,59]

$$dO_{\sigma/\pi}(r) = O_{\sigma/\pi}(r) - k_{\sigma/\pi}dr^2/2, \tag{B34}$$

$$f_{\sigma/\pi}(r) = -r/[l_c dO_{\sigma/\pi}(r)/dr] = 1/[l_c k_{\sigma/\pi}]. \tag{B35}$$

$f_{\sigma/\pi}$ are the focal lengths for σ and π polarization, respectively. In contrast to the commonly used equation $f(r)=-1/[l_c d^2O(r)/dr^2]$, Eq. (B35) also describes the thermal lens correctly, if Eq. (B34) includes an aspheric part, e.g., a term $\sim dr^4$. Solving Eq. (B34) for k, replacing r by x or y, using the discrete notation of the finite-element approach, and fitting a spherical lens to the difference in optical path length between two elements, we can write (e.g., for the tangential resonator plane)

$$k_{\sigma/\pi,x}=2[O_{\sigma/\pi}(x_1)-O_{\sigma/\pi}(x_2)]/[x_2^2-x_1^2], \quad \text{(B36)}$$

$$f_{\sigma/\pi}(x)=-x/[l_c dO_{\sigma/\pi}(x)/dx]$$
$$=[x_2^2-x_1^2]/\{2l_c[O_{\sigma/\pi}(x_1)-O_{\sigma/\pi}(x_2)]\}. \quad \text{(B37)}$$

We further calculate single (i.e., not transversely resolved) values of the thermal lens power by weighting the transverse shape of the thermal lens power with the Gaussian intensity shape of the laser or probe beam which was used for the thermal lens measurements.

*Present address: Department of Chemistry and Biochemistry, University of Bern, Freiestrasse 3, CH-3012 Bern, Switzerland.
FAX: ++41-31-631 43 99.
Electronic address: pollnau@iac.unibe.ch

[1] J. E. Murray, IEEE J. Quantum Electron. **19**, 488 (1983).
[2] T. M. Pollak, W. F. Wing, R. J. Grasso, E. P. Chicklis, and H. P. Jenssen, IEEE J. Quantum Electron. **18**, 159 (1982).
[3] H. Vanherzeele, Opt. Lett. **13**, 369 (1988).
[4] G. Cerullo, S. de Silvestri, and V. Magni, Opt. Commun. **93**, 77 (1992).
[5] T. Y. Fan, G. J. Dixon, and R. L. Byer, Opt. Lett. **11**, 204 (1986).
[6] W. Seelert, H. P. Kortz, and W. M. Yen, in *Proceedings on Advanced Solid-State Lasers*, edited by L. L. Chase and A. A. Pinto (Optical Society of America, Washington, D.C., 1992), Vol. 13, p. 209.
[7] R. Beach, P. Reichert, W. Benett, B. Freitas, S. Mitchell, A. Velsko, J. Darwin, and R. Solarz, Opt. Lett. **18**, 1326 (1993).
[8] Y. Guyot, H. Manaa, J. Y. Rivoire, R. Moncorgé, N. Garnier, E. Descroix, M. Bon, and P. Laporte, Phys. Rev. B **51**, 784 (1995).
[9] T. Chuang and H. R. Verdún, IEEE J. Quantum Electron. **32**, 79 (1996).
[10] M. Pollnau, P. J. Hardman, W. A. Clarkson, and D. C. Hanna, Opt. Commun. **147**, 203 (1998).
[11] P. J. Hardman, M. Pollnau, W. A. Clarkson, and D. C. Hanna, in *UK National Quantum Electronics Conference QE-13*, Technical Digest (Institute of Physics, London, 1997), p. 132; P. J. Hardman, W. A. Clarkson, G. J. Friel, M. Pollnau, and D. C. Hanna, IEEE J. Quantum Electron. (to be published).
[12] H. G. Danielmeyer, M. Blätte, and P. Balmer, Appl. Phys. **1**, 269 (1973).
[13] D. P. Devor, L. G. DeShazer, and R. C. Pastor, IEEE J. Quantum Electron. **25**, 1863 (1989).
[14] T. Y. Fan, IEEE J. Quantum Electron. **29**, 1457 (1993).
[15] V. Lupei and A. Lupei, Opt. Eng. (Bellingham) **35**, 1252 (1996).
[16] M. Pollnau, W. A. Clarkson, and D. C. Hanna, in *Conference on Lasers and Electro-Optics*, Vol. 6, OSA Technical Digest Series (Optical Society of America, Washington, D.C., 1998), p. 100.
[17] A. V. Mezenov, L. N. Soms, and A. I. Stepanov, J. Sov. Laser Res. **8**, 427 (1987).
[18] M. E. Innocenzi, H. T. Yura, C. L. Fincher, and R. A. Fields, Appl. Phys. Lett. **56**, 1831 (1990).
[19] S. C. Tidwell, J. F. Seamans, M. S. Bowers, and A. K. Cousins, IEEE J. Quantum Electron. **28**, 997 (1992).
[20] A. K. Cousins, IEEE J. Quantum Electron. **28**, 1057 (1992).
[21] J. Frauchiger, P. Albers, and H. P. Weber, IEEE J. Quantum Electron. **28**, 1046 (1992).
[22] N. Hodgson and H. Weber, IEEE J. Quantum Electron. **29**, 2497 (1993).
[23] C. Pfistner, R. Weber, H. P. Weber, S. Merazzi, and R. Gruber, IEEE J. Quantum Electron. **30**, 1605 (1994).
[24] U. Brauch, Appl. Phys. B: Lasers Opt. **58**, 397 (1994).
[25] L. Yan and C. H. Lee, J. Appl. Phys. **75**, 1286 (1994).
[26] M. Bode, M.S. thesis, Laser Zentrum Hannover, Hannover, Germany, 1995.
[27] W. Koechner, *Solid-State Laser Engineering*, 4th ed., Springer Series in Optical Science Vol. 1 (Springer-Verlag, Berlin, 1996), Chap. 7.
[28] W. A. Clarkson and D. C. Hanna, Opt. Lett. **21**, 375 (1996).
[29] V. Lupei, A. Lupei, S. Georgescu, and C. Ionescu, Opt. Commun. **60**, 59 (1986).
[30] V. Lupei, A. Lupei, S. Georgescu, C. Ionescu, and W. M. Yen, J. Lumin. **39**, 35 (1987).
[31] B. Viana, A. M. Lejus, D. Saber, N. Duxin, and D. Vivien, Opt. Mater. **3**, 307 (1994).
[32] B. Comaskey, B. D. Moran, G. F. Albrecht, and R. J. Beach, IEEE J. Quantum Electron. **31**, 1261 (1995).
[33] D. C. Brown, IEEE J. Quantum Electron. **34**, 560 (1998).
[34] S. Guy, C. L. Bonner, D. P. Shepherd, D. C. Hanna, A. C. Tropper, and B. Ferrand, IEEE J. Quantum Electron. **34**, 900 (1998).
[35] D. C. Brown, IEEE J. Quantum Electron. **33**, 861 (1997).
[36] N. W. Ashcroft and N. D. Mermin, *Solid State Physics* (Sounders College, Philadelphia, 1976), Chap. 25 (international edition).
[37] G. A. Slack and D. W. Oliver, Phys. Rev. B **4**, 592 (1971).
[38] B. W. Woods, S. A. Payne, J. E. Marion, R. S. Hughes, and L. E. Davis, J. Opt. Soc. Am. B **8**, 970 (1991).
[39] W. Koechner, *Solid-State Laser Engineering*, 4th ed., Springer Series in Optical Science Vol. 1 (Springer-Verlag, Berlin, 1996), Chap. 2.
[40] D. S. Sumida, D. A. Rockwell, and M. S. Mangir, IEEE J. Quantum Electron. **24**, 985 (1988).
[41] E. G. Spencer, R. T. Denton, T. B. Bateman, W. B. Snow, and L. G. Van Uitert, J. Appl. Phys. **34**, 3059 (1963).
[42] A. A. Kaminskii, *Laser Crystals*, Springer Series in Optical Science Vol. 14 (Springer-Verlag, Berlin, 1981).
[43] P. H. Klein and W. J. Croft, J. Appl. Phys. **38**, 1603 (1967).
[44] J. R. Ryan and R. Beach, J. Opt. Soc. Am. B **9**, 1883 (1992).
[45] J. D. Zuegel and W. Seka, IEEE J. Quantum Electron. **31**, 1742 (1995).
[46] C. Bibeau, S. A. Payne, and H. T. Powell, J. Opt. Soc. Am. B **12**, 1981 (1995).
[47] C. Li, Y. Guyot, C. Linarès, R. Moncorgé, and M. F. Joubert, in *Advanced Solid-State Lasers and Compact Blue-Green Lasers*, Technical Digest (Optical-Society of America, Washington, D.C., 1993), Vol. 2, p. 423.
[48] W. F. Krupke, IEEE J. Quantum Electron. **7**, 153 (1971).

[49] M. Pollnau, Th. Graf, J. E. Balmer, W. Lüthy, and H. P. Weber, Phys. Rev. A **49**, 3990 (1994).
[50] A. E. Siegman, *Lasers* (University Science Books, Mill Valley, CA, 1986), Chap. 7.
[51] M. Malinowski, B. Jacquier, M. Bouazaoui, M. F. Joubert, and C. Linares, Phys. Rev. B **41**, 31 (1990).
[52] U. O. Farrukh and P. Brockman, Appl. Opt. **32**, 2075 (1993).
[53] W. J. Alton and A. J. Barlow, J. Appl. Phys. **38**, 3023 (1967).
[54] T. K. Gupta and J. Valentich, J. Am. Ceram. Soc. **54**, 355 (1971).
[55] T. M. Pollak, R. C. Folweiler, E. P. Chicklis, J. W. Baer, A. Linz, and D. Gabbe, Natl. Bur. Stand. (U.S.) Spec. Pub. 568 (Natl. Bur. Stand., Washington, D.C., 1980), p. 127.
[56] H. S. Carslaw and J. C. Jaeger, *Conduction of Heat in Solids* (Oxford University Press, Oxford, 1959).
[57] Y. S. Touloukian, *Thermophysical Properties of Matter* (Plenum, New York, 1972), Vol. 2.
[58] M. A. Kern, W. A. Clarkson, and D. C. Hanna, in *Conference on Lasers and Electro-Optics*, Vol. 11, OSA Technical Digest Series (Optical Society of America, Washington, D.C., 1997), p. 479.
[59] M. A. Kern, M.S. thesis, Institute of Laser-Physics, University of Hamburg, Germany, 1997.